

Biaxial Strain Control of Helimagnetism via Chemical Expansion in Thin Film SrFeO₃

J. Fowlie,^{1, 2,*} J. Li,^{1, 2} D. Puggioni,³ L. Barreto,^{4, 5, 6} L. Yuan,³ J. M. Rondinelli,³ R. Sutarto,⁷ T. D. Boyko,⁷ F. Orlandi,⁸ P. Manuel,⁸ D. D. Khalyavin,⁸ E. G. Lomeli,^{1, 9} B. Moritz,¹ T. P. Devreux,^{1, 9} S. Koroluk,¹⁰ R. J. Green,^{10, 11} S. J. May,¹² and H. Y. Hwang^{1, 2}

¹Stanford Institute for Materials and Energy Sciences,

SLAC National Accelerator Laboratory, Menlo Park, CA 94025, USA

²Department of Applied Physics, Stanford University, Stanford, CA 94305, USA

³Department of Materials Science and Engineering,
Northwestern University, Evanston, IL 60208, USA

⁴Singh Center for Nanotechnology, University of Pennsylvania, Philadelphia, PA 19104, USA

⁵Center for Natural Sciences and Humanities, Federal University of ABC - UFABC, Santo André 09210-580, SP, Brazil

⁶Department of Physics, University of Johannesburg,
PO Box 524, Auckland Park, 2006, South Africa

⁷Canadian Light Source, Saskatoon, SK S7N 2V3, Canada

⁸ISIS Neutron and Muon Source, STFC Rutherford Appleton Laboratory,
Harwell Campus, Didcot, Oxfordshire OX11 0QX, United Kingdom

⁹Department of Materials Science and Engineering, Stanford University, Stanford, CA 94305, USA

¹⁰Department of Physics & Engineering Physics,
University of Saskatchewan, Saskatoon, Canada S7N 5E2

¹¹Stewart Blusson Quantum Matter Institute, University of British Columbia, Vancouver, Canada V6T 1Z4

¹²Department of Materials Science and Engineering,
Drexel University, Philadelphia, Pennsylvania 19104, USA

(Dated: February 12, 2026)

We demonstrate control of helimagnetic order in biaxially strained SrFeO₃ thin films using neutron diffraction and resonant soft x-ray scattering. SrFeO₃, a negative charge-transfer oxide, exhibits a complex magnetic phase diagram that includes multi-q spin structures. Tensile epitaxial strain produces a pronounced shortening of the helimagnetic ordering length and a tilting of the magnetic ordering vector. We interpret this behavior in terms of chemical expansion: lattice dilation under tensile strain lowers the energetic cost of oxygen vacancies, leading to an expanded unit cell that modifies Fe–O hybridization and enhances superexchange relative to double exchange. These results reveal how epitaxial strain can indirectly tune helimagnetism through defect-driven chemical expansion, highlighting the strong coupling between lattice, chemistry, and magnetic order in transition-metal oxides. Our findings establish chemical expansion as an effective mechanism for engineering complex magnetic textures in oxide thin films, with implications for spintronic, magnonic, and quantum information applications.

I. INTRODUCTION

Helimagnets are a class of magnetically ordered materials in which local moments arrange in a spiral or a helical pattern. Despite having no *net* magnetization, these systems can potentially host chiral spin textures, and, in multi-q helimagnets, topologically-protected magnetic structures. As a result, helimagnets are gaining interest for potential spintronic and magnonic components [1] as well as future qubit platforms [2]. They may also exhibit non-relativistic spin-momentum coupling with p-wave symmetry [3, 4].

Helimagnetism typically arises in magnetic systems where the crystalline structure breaks inversion symmetry. This is the case in B20 structures, where a Dzyaloshinskii–Moriya interaction (DMI) emerges and the helimagnetic ordering length can be tens of nanometers [5, 6]. Helimagnetism can also occur in centrosymmetric crystals, i.e.,

without the magnetic chirality being locked to the underlying crystal chirality. In these cases, the helimagnetism may stem from a geometric frustration of the magnetic order and the ordering length is typically much shorter, only a few nanometers [7]. SrFeO₃ is an example of a helimagnetic compound that is centrosymmetric and cubic, so its helimagnetism cannot be explained by either DMI physics or geometric frustration [8], but, rather, may arise from the competition between exchange interactions [9]. The higher symmetry of the chemical unit cell, as well as the metallicity of SrFeO₃, make it an attractive material for a future reconfigurable magnetic component.

The helimagnetic order in SrFeO₃ is aligned approximately along the [1 1 1] direction and has an incommensurate length of 17–18 Å. SrFeO₃ is reported to have multiple helimagnetic phases as a function of temperature [10–12]. Ishiwata and coworkers recently proposed that SrFeO₃ hosts a double-q state (proper screw and cycloid) at low temperature and a quadruple-q state (4 × proper screw) for 80 K \lesssim T \lesssim 120 K, the latter of which is speculated to host a topologically-protected three-dimensional skyrmion lattice [13]. The characteristic length scale of

* jfowlie@northwestern.edu; Now at Department of Materials Science and Engineering, Northwestern University

these magnetic textures is expected to be on the order of 5 nm, while the helimagnetic pitch itself is shorter than 2 nm [13]. These exceptionally short length scales make direct real-space imaging of the magnetic order in SrFeO_3 particularly challenging.

The leading theory for the origin of helimagnetism in SrFeO_3 is based on characteristics of its electronic structure [9]. Nominally, SrFeO_3 is high spin d^4 , and calculated to be nearly half-metallic [14]. Experimentally, SrFeO_3 exhibits significant charge transfer character [15]. The transfer of electrons from oxygen to iron make it closer to $d^5 \underline{L}$ [16], where \underline{L} denotes an oxygen ligand hole. X-ray spectroscopy measurements suggest a $d^5 \underline{L}$ portion as high as 90% [17] while recent multiplet calculations reveal greater than 60% of the $d^5 \underline{L}$ character is Fe high spin $S = 5/2$ configuration with an antiparallel oxygen $S = 1/2$ [18]. It has been suggested that, in this negative charge transfer energy regime, the interaction between localized electronic moments and itinerant oxygen holes leads to the preferential helimagnetic order [9, 19].

Going from bulk to thin film samples introduces a symmetry lowering and biaxial strain, which may influence the electronic structure, and therefore the helimagnetism. From existing literature, helimagnetic, spiral magnet, chiral magnet, or skyrmion lattice compounds respond to the thin film environment in complex and distinct ways depending on the underlying physics. In conventional DMI-mediated B20 materials, imposing thin film geometry is reported to extend the temperature and field parameter space over which the skyrmion lattice is observed [20–22]. This is suggested to be due to induced magnetic anisotropy and is supported by uniaxial pressure studies on single crystals [23]. In B20 compounds, hydrostatic pressure has also been observed to cause a shortening of the chiral magnetic ordering length [24] and a reorientation of the ordering vector, attributed to enhanced electron itinerancy [25]. In multiferroic spiral magnets, the strong magnetoelastic coupling provides a direct path for strain-induced modifications to the magnetic order. For instance, in BiFeO_3 the spin cycloid is suppressed in favor of a collinear magnetic order when biaxial strain is high and either tensile or compressive [26]. In cobalt-doped BiFeO_3 thin films, the spiral ordering length is also observed to increase significantly with decreasing thickness [27]. In TbMnO_3 , the incommensurate cycloid shortens and becomes commensurate under compressive biaxial strain [28].

The physics underlying the helimagnetism of SrFeO_3 is expected to be distinct from either B20 or multiferroic compounds because SrFeO_3 is centrosymmetric and thus, to leading order, lacks DMI and significant magnetoelastic coupling. Exploration of the effect of the thin film environment on a centrosymmetric helimagnet has, to our knowledge, not been reported. Here we show, using neutron and X-ray scattering, that the helimagnetic ordering is strongly affected by the biaxial strain imposed by the substrate in SrFeO_3 thin films. Specifically, we first report that the thin film environment preferentially selects a mag-

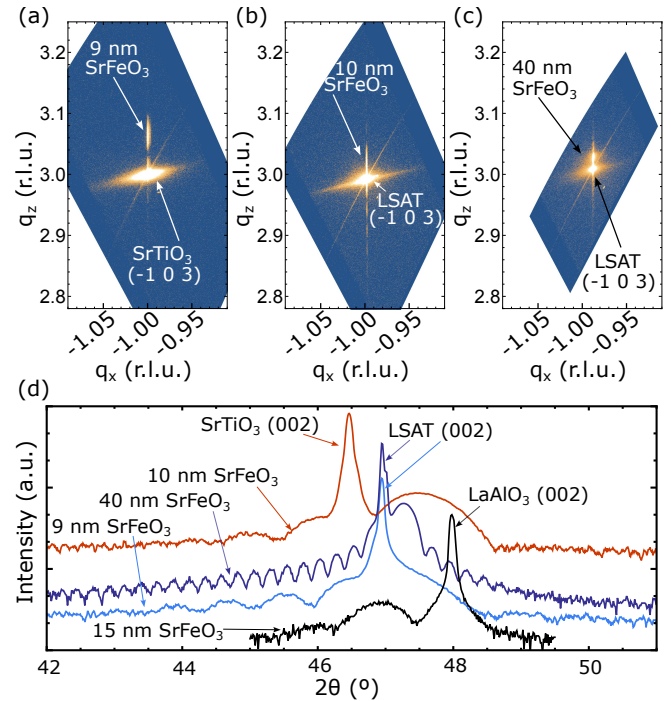


FIG. 1. a)-c) Reciprocal space maps around the $(-1 \ 0 \ 3)$ peak of the substrate: (a) 9 nm PLD-grown $\text{SrFeO}_3/\text{SrTiO}_3$, (b) 10 nm PLD-grown $\text{SrFeO}_3/\text{LSAT}$ and (c) 40 nm PLD-grown $\text{SrFeO}_3/\text{LSAT}$. d) $(0 \ 0 \ 2)$ peak θ - 2θ measurements of 15 nm MBE-grown $\text{SrFeO}_3/\text{LaAlO}_3$ (black), 10 nm PLD-grown $\text{SrFeO}_3/\text{LSAT}$ (light blue) and 9 nm PLD-grown $\text{SrFeO}_3/\text{SrTiO}_3$ (red) used for synchrotron x-ray measurements and 40 nm PLD-grown $\text{SrFeO}_3/\text{LSAT}$ used for neutron scattering (dark blue).

netic domain where the helimagnetic ordering vector tilts towards the more compressed direction. We then show that the helimagnetic real-space ordering length decreases as the unit cell volume increases, in contrast to the effects of strain or pressure on B20 or multiferroic helimagnetic compounds. Such a shortening may be explained by a relative enhancement of the superexchange interaction over the double exchange interaction. Our density functional theory (DFT) calculations show that the shortening is unlikely to be caused by the direct strain effect and instead may stem from a strain-induced shift in the chemical potential driven by oxygen stoichiometry. In order to demonstrate the robustness of our findings across different samples, we study SrFeO_3 thin films grown and annealed in different oxidising environments: SrFeO_3 grown by pulsed laser deposition (PLD) and post-annealed in ozone and SrFeO_3 grown by molecular beam epitaxy (MBE) and post annealed in oxygen plasma.

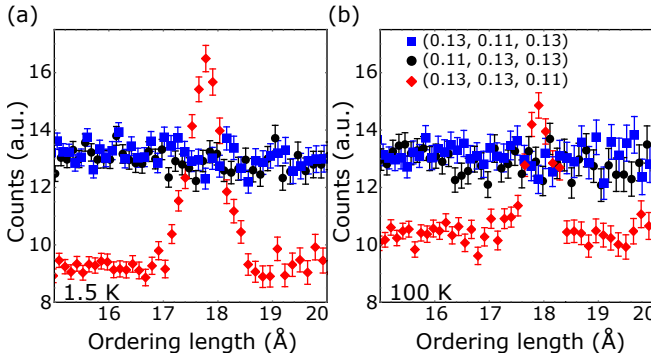


FIG. 2. d -spacing neutron diffraction data around the magnetic Bragg peak of SrFeO_3 . (a) At 1.5 K and (b) at 100 K. Both panels show integrated intensity within three regions of reciprocal space that are equivalent in cubic symmetry; (0.13, 0.11, 0.11), (0.11, 0.13, 0.13) and (0.13, 0.13, 0.11).

II. EXPERIMENT

A. Sample preparation

Thin film samples were grown by PLD or MBE and post-processed according to the procedure outlined in Methods. Substrates are (001)-oriented SrTiO_3 , (001)-oriented $(\text{LaAlO}_3)_{0.3}(\text{Sr}_2\text{AlTaO}_6)_{0.7}$ (LSAT) and (001)-oriented LaAlO_3 . For synchrotron soft x-ray scattering we prepared: 9 nm $\text{SrFeO}_3/\text{SrTiO}_3$ and 10 nm $\text{SrFeO}_3/\text{LSAT}$ grown by PLD and 15 nm $\text{SrFeO}_3/\text{LaAlO}_3$, 15 nm $\text{SrFeO}_3/\text{LSAT}$, and 14 nm $\text{SrFeO}_3/\text{SrTiO}_3$ grown by MBE. We also prepared eight equivalent 40 nm $\text{SrFeO}_3/\text{LSAT}$ samples by PLD for neutron diffraction. SrFeO_3 has a bulk lattice parameter of approximately 3.85 Å and LSAT has a lattice parameter of 3.87 Å, so LSAT provides a slightly tensile strain of 0.4 %.

Fig. 1 shows characterization by in-house x-ray diffraction reciprocal space maps (RSMs) and θ - 2θ measurements. RSMs indicate that the films are fully epitaxially strained. θ - 2θ scans show finite thickness oscillations, suggesting a high crystalline quality of the epitaxial SrFeO_3 . Table I summarizes relevant structural parameters for the samples discussed in this work, as well as bulk samples reported previously [8]. The c-axis (out-of-plane, or along the surface normal) lattice parameters have been obtained from the θ - 2θ scans.

B. Neutron diffraction

In order to achieve a sufficient sample volume for neutron scattering, eight SrFeO_3 samples were prepared (see Methods) on 5×5 mm LSAT substrates, with a film thickness of 40 nm giving a total sample volume of 8×10^{-3} mm³. The samples were then mounted in a mosaic, aligned relative to each other within an azimuthal angle of 1°, for neutron experiments carried out at the WISH

diffractometer at the ISIS Neutron Source [29].

Fig. 2 shows the diffraction focused neutron data as a function of d -spacing at the position $(0,0,0)+k$, where $k = (0.13, 0.13, 0.11), (0.13, 0.11, 0.13), (0.11, 0.13, 0.13)$. Panel a) is data recorded at 1.5 K and panel b) is data recorded at 100 K. The ordering length of ≈ 17.8 Å is consistent with previous reports. In both panels, three curves are shown, corresponding to three regions of reciprocal space where equivalent peaks, related by threefold symmetry, would be expected in a cubic structure. The Miller indices corresponding to the Bragg peaks were calculated absolutely from an orientation matrix based on the LSAT structural peaks that were visible in the same detector image. The same peak is observed on a single sample rather than a mosaic, as shown in Fig. S1 in the Supplementary Information (SI). The same indexation of the magnetic peaks has been obtained in both cases confirming that the mosaic spread does not affect the determination of the propagation vector.

The magnetic Bragg peak observed is (0.13 0.13 0.11). The observation that the ordering is tilted slightly away from the [1 1 1] direction was previously reported by Ishiwata and co-workers in the low temperature, double- q state, who observed three peaks of the form (q, q, q') , (q, q', q) , and (q', q, q) where $q' > q$ [13]. Compared to those bulk reports we see three differences: 1) the peak we observe is of the form (q, q, q') but with $q > q'$. 2) We do not observe the peaks (q, q', q) and (q', q, q) . 3) The same authors report that above 80 – 90 K the ordering is uniquely along the high symmetry [1 1 1] direction. This is not the case in our experiment and the peak remains at (0.13, 0.13, 0.11).

Considering magnetic symmetry, even with these three differences, our observations are not inconsistent with the symmetries determined by Ishiwata and coworkers. Our low temperature (Phase I) magnetic structure is consistent with at least two domains of double- q ordering. Ishiwata and coworkers interpreted their Phase II magnetic structure as a single domain of a quadruple- q order. Our data is consistent with this, but in their case the propagation vector is along the high symmetry [1 1 1] direction so the magnetic structure retains cubic symmetry while our Phase II magnetic structure must have, at most, tetragonal symmetry.

The (0.13, 0.13, 0.11) peak that we observe corresponds to a tilting of the magnetic ordering vector away from the [1 1 1] direction more out of the plane of the sample. Due to the tensile strain, the out-of-plane direction is more compressed. Although biaxial strain breaks the symmetry between the in-plane and out-of-plane directions, it is notable that the system so strongly prefers only one of the three ordering directions since the strain is moderate and the films are relatively thick. This suggests a strong sensitivity of the helimagnetic order to the biaxial strain.

	Bulk	LaAlO ₃ (MBE)	LSAT (MBE)	SrTiO ₃ (MBE)	LSAT (PLD)	SrTiO ₃ (PLD)
a,b-parameter	3.85 Å	3.79 Å	3.87 Å	3.905 Å	3.87 Å	3.905 Å
c-parameter	3.85 Å	3.876 Å	3.831 Å	3.81 Å	3.84 Å	3.81 Å
Epitaxial strain	0%	-1.6%	+0.4%	+1.4%	+0.4%	+1.4%
Unit cell volume	57.07 Å ³	55.68 Å ³	57.37 Å ³	58.10 Å ³	57.57 Å ³	58.10 Å ³
[111] diagonal length	6.67 Å	6.61 Å	6.68 Å	6.71 Å	6.69 Å	6.71 Å

TABLE I. Unit cell a, b, and c lattice parameters, epitaxial strain, unit cell volume, and [1 1 1] body diagonal length for SrFeO₃ in bulk [8], and as a thin film grown on LaAlO₃, LSAT, and SrTiO₃ by PLD and by MBE. All values are reported at room temperature.

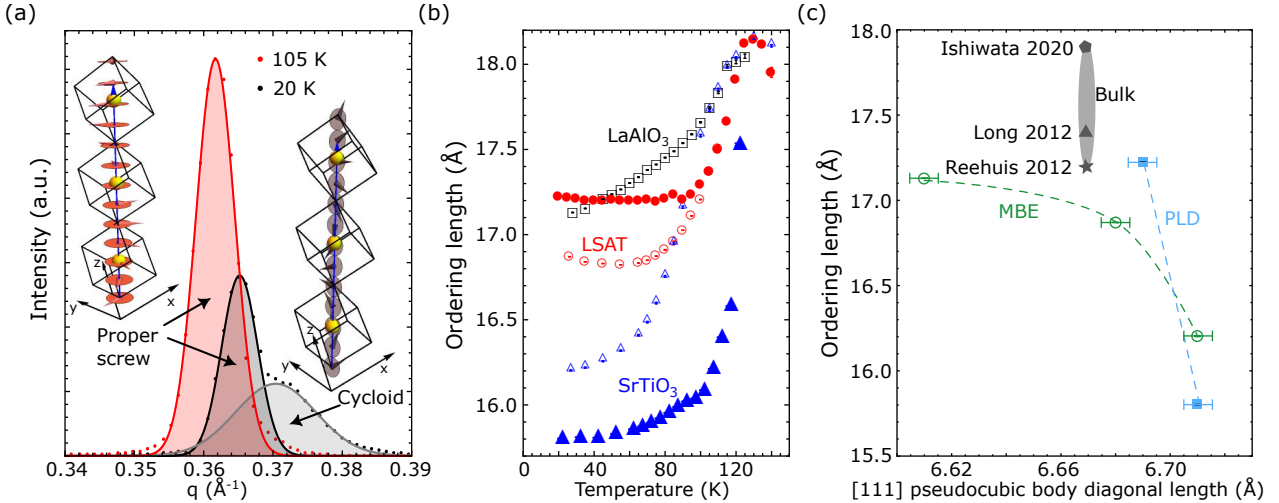


FIG. 3. Resonant soft x-ray scattering data recorded on the Fe L₃ edge in linear horizontal (π) polarization. (a) θ - 2θ scans across the magnetic Bragg peak of PLD-grown SrFeO₃/LSAT. The 20 K (black) and 105 K (red) data are shown. The more intense peak corresponds to the proper screw order, while the less intense peak corresponds to a spin cycloid. Shaded regions are for illustrative purposes and are not numerical fits. Insets sketch the different spiral structures where the incommensurate ordering vector is shown in blue and iron atoms in the body center positions are indicated by yellow spheres. (b) The proper screw ordering length extracted from the θ - 2θ scans as a function of temperature. PLD-grown samples are represented by filled shapes while MBE-grown samples are represented by empty shapes. Error bars (often smaller than the plot marker) represent one standard deviation from the center of a Gaussian lineshape. (c) The base temperature (≈ 20 K) ordering length of the proper screw structure as a function of the [111] body diagonal length of the chemical unit cell for the two series of sample. A survey of bulk values are represented by the gray plot markers [13, 30, 31]. For consistency, body diagonal length is calculated from room temperature lattice parameters – SrFeO₃ exhibits only a weak thermal contraction of $\approx -0.25\%$ from room temperature to 100 K [8]. Horizontal error bars represent a ± 0.005 Å tolerance on the unit cell diagonal while vertical error bars are smaller than the plot markers. The dashed lines are guides to the eye.

C. Resonant soft x-ray scattering

Resonant soft x-ray scattering (RSXS) measurements were carried out at the REIXS beamline of the Canadian Light Source. The samples were mounted on a wedge to bring the [111] direction into the diffraction plane. All measurements were θ - 2θ scans around the position of the magnetic Bragg peak conducted with a beam energy resonant with the Fe L₃ edge at around 708 eV. Fig. 3a presents a subset of the data at 20 K and at 100 K for PLD-grown SrFeO₃/LSAT. The full set of measurements for all samples and temperatures are presented in Fig. S2 in the SI. At low temperatures there are two peaks observed for some samples. It is deduced from linear dichroism (see SI Fig. S3) that the peak at higher momentum transfer,

q , (shorter ordering length) is a cycloidal spiral while the more intense peak at lower q (longer ordering length) is a proper screw. We note that our neutron scattering experiment does not resolve the separation between the two peaks but, as shown in SI Fig. S1, the width is consistent with the two close peaks observed in RSXS. At intermediate temperatures there is only one peak clearly observed in all samples, deduced to be of proper screw structure. The data obtained is consistent with Ishiwata and coworkers' neutron diffraction reports on bulk single crystal samples, but to our knowledge, this is the first confirmation of an equivalent multi- q ground state in thin film samples.

Fig. 3b plots the ordering length as a function of temperature for the full data set. Only the peak arising from

the proper screw structure is plotted for simplicity but both peaks have the same trend with temperature. The ordering length increases with increasing temperature for all SrFeO_3 samples, until, around 120 K, the magnetic Bragg peak is extinguished and SrFeO_3 becomes paramagnetic. Finally, Fig. 3c shows the proper screw ordering length as a function of the pseudocubic unit cell body diagonal as stated in Table I. In the samples with two peaks, the cycloidal spiral has the same trend with strain as the proper screw, as can be seen in SI Fig. S2. The proper screw ordering length decreases on the order of 10% when the unit cell is expanded by tensile biaxial strain by approximately only 1%. This is an extreme strain effect.

III. THEORY

From both our neutron diffraction and our resonant soft x-ray diffraction results we see that the incommensurate helimagnetic spiral of SrFeO_3 extends when the lattice is more compressed, and contracts significantly when tensile strain causes the unit cell to expand. We now discuss the possible origins with support from first principles DFT (see Methods).

In the extreme, long wavelength helimagnetic order (small helimagnetic angle) begins to resemble ferromagnetic order, while short helimagnetic order begins to resemble antiferromagnetic order (collinear from a spin cycloid and non-collinear from a proper screw). In these terms, the magnetic ordering in SrFeO_3 moves closer to an antiferromagnetic ground state when the lattice is expanded and closer to a ferromagnetic ground state when the lattice is compressed. This is consistent with Mössbauer spectroscopy results showing that under a hydrostatic pressure of 13 GPa, where the lattice is more compressed, SrFeO_3 transitions to a fully ferromagnetic ground state [32]. According to the model developed by Mostovoy [9], helimagnetic order arises from a competition between the kinetic energy of itinerant, hybridized Fe–O p – d bands and the covalent energy gain associated with p – d hybridization. Although this mechanism is formulated in terms of band energetics rather than localized exchange interactions, its magnetic consequences are commonly interpreted in terms of an effective competition between double-exchange (DE)-like (kinetic) and superexchange (SE)-like (covalent) tendencies [19, 33]. In this effective picture, the DE-like contribution favors long-wavelength (ferromagnetic-like) order, whereas the SE-like contribution favors shorter-wavelength (antiferromagnetic-like) order, consistent with the evolution of the helimagnetic ordering length.

First, we consider the electronic structure of pristine SrFeO_3 under strain. Fig. 4a shows the ordering length dependence of the total energy difference between the helimagnetic ordering along the [111] direction and the ferromagnetic state, evaluated for various epitaxial strains. Across the full strain range, from -1.6% compressive

(LaAlO_3) to +1.4% tensile (SrTiO_3), the helical [111] configuration is consistently lower in energy than the ferromagnetic state, indicating that it is generally favorable. The position of the energy minimum determines the helimagnetic ordering length (Fig. 4b), and indicates that it increases with tensile strain. This result can be understood by considering the direct effect of strain on the electronic structure. Briefly, tensile strain on negative charge transfer SrFeO_3 reduces the orbital overlap between the iron 3d e_g states and oxygen p states, quantified by the integral $p d\sigma$. DE scales approximately as $\frac{(p d\sigma)^2}{\Delta}$, where Δ is the charge-transfer energy. SE scales as $\frac{(p d\sigma)^4}{U \Delta^2}$, where U is the on-site Coulomb repulsion of the Fe 3d states [34–38]. Tensile strain thus suppresses SE more strongly than DE. As a result, DE becomes relatively more dominant, leading to a lengthening of the helimagnetic ordering. Considering only the direct effect of strain on the p – d hopping integral is thus not sufficient to explain the trend observed experimentally.

It is possible that a secondary electronic effect that is not captured by our DFT calculations can account for the experimental trend of decreasing helimagnetic ordering length with increasing tensile strain. Parameters such as the Hund's energy, J_H , or the crystal field splitting may play a more complex role as a function of strain in this correlated material. Biaxial strain alters the crystal field via changes in Fe–O bond lengths and symmetry. However, these effects are already considered in the hopping integrals. Hund's coupling J_H , being largely atomic, is not expected to vary significantly with strain. Furthermore, we find that the preferential ordering length is largely unaffected by the J_H/U ratio (with $U = 3$ eV; see SI Fig. S4).

To account for both the direction and magnitude of the helimagnetic ordering length trend with strain, we consider chemical modifications to SrFeO_3 . Despite the formal Fe^{4+} valence, strong Fe–O covalency places SrFeO_3 in the negative charge-transfer regime. The DFT occupation matrix yields an Fe 3d filling close to d^6 (see SI Tab. S1), reflecting significant Fe 3d–O 2p hybridization rather than a purely atomic valence. Accordingly, O 2p states dominate at the Fermi level (see SI Fig. S5), consistent with a covalent $d^5 \underline{L}$ description. Due to this electronic configuration, the formation of oxygen vacancies mainly removes the ligand hole rather than destabilizing the Fe sublattice. This reduces the energy cost of vacancy formation and makes oxygen non-stoichiometry readily accommodated in SrFeO_3 [39]. Tensile strain then further promotes vacancy formation – not only because vacancies relax the lattice misfit, but also because the local lattice expansion associated with vacancy formation partially offsets the out-of-plane contraction imposed by in-plane expansion [40–42]. On the other hand, compressive strain has a much weaker effect on the formation energy of oxygen vacancies [42]. In this work, we do not model oxygen vacancies explicitly; instead, we capture the electronic effect of oxygen deficiency by tuning the total number of electrons, thereby simulating the associated carrier doping

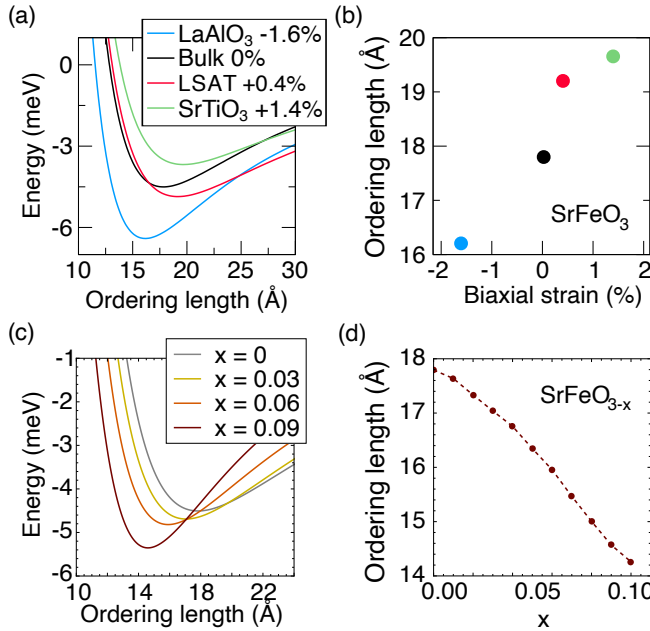


FIG. 4. Strain dependence of the [111] helimagnetic ordering length from DFT for (a,b) pristine SrFeO₃ and (c,d) oxygen deficient bulk SrFeO_{3-x}. (a, c) display the total energy difference between the helimagnetic state (propagating along [111]) and the ferromagnetic state while (b, d) display the ordering length as a function of strain and x respectively.

[43].

Our DFT calculations shown in Fig. 4c,d (also see SI Fig. S6) show that in SrFeO_{3-x} ($0 \leq x \leq 0.1$) the magnetic ordering length decreases systematically with increasing oxygen vacancy concentration x . To investigate the origin of this effect, we computed the overlap integral S and the center of mass (COM) for Fe e_g and O $2p$ states in oxygen-deficient bulk SrFeO_{3-x} (see SI Tab. S2). In the occupied states, S increases for both spin channels (e.g., S^\uparrow : 1.373 \rightarrow 1.410), and the COM of both orbitals shifts slightly downward, reflecting enhanced Fe(e_g)-O($2p$) p - d hybridization and modest stabilization of the occupied states. Changes in the unoccupied states are minimal. The enhanced Fe–O hybridization at $x = 0.1$ indicates that electron doping associated with oxygen vacancies primarily redistributes electronic spectral weight within the occupied states. This enhanced p - d hybridization promotes superexchange interactions over double exchange interactions, consistent with the Mostovoy model [9], thereby favoring shorter helimagnetic ordering as the oxygen vacancy concentration increases.

Considering this evidence, the experimental trend of the helimagnetic ordering length can be reproduced by assuming an increasing effective density of electrons from compressive (LaAlO₃) to tensile (SrTiO₃) strain conditions, as shown in Fig. 4b. This suggests that the strain-dependent redistribution of vacancy-induced charge carriers, rather than strain alone, plays a central role in determining the helical period.

IV. DISCUSSION AND CONCLUSION

We find that the [111] helimagnetic ordering in SrFeO₃ is sensitive to biaxial strain, tilting slightly off the [111] vector in the compressed direction, and exhibiting a real-space contraction on the order of 10% with an expansion of the [111] unit cell body diagonal on the order of only 1%. The sign of the strain trend is counter to that observed in B20 or multiferroic helimagnets and inconsistent with theory from both model Hamiltonian and first principles calculations. Instead, we propose that the extreme strain effect is chemically-mediated.

Tensile strain is known to promote the formation of oxygen vacancies [42], consistent with, and reciprocal to, the established concept of chemical expansion, whereby oxygen vacancy formation produces a positive chemical strain, in this case further driven by the energetically-favorable reduction of Fe⁴⁺ toward Fe³⁺ [44]. Our DFT calculations show that oxygen loss as low as 3% is enough to reproduce both the magnitude and direction of the strain effect on the helimagnetic ordering length.

We briefly compare our findings to previous studies on chemical modifications of SrFeO₃. 1) Beyond the oxygen off-stoichiometries of a few percent considered here, strontium iron oxides are also stabilized in various oxygen ordered phases. Sr₈Fe₈O₂₃ (SrFeO_{2.87}) exhibits helimagnetism with an ordering length of 11 Å [30]. Although the departure from cubic symmetry introduces distinct iron sites and magnetic anisotropy, it is interesting that the loss of oxygen also leads to a shorter helix. Highly oxygen deficient, but not oxygen-ordered, SrFeO_x with $x = 2.68$ is not observed to be helimagnetic [45]. 2) The compound La_{1/3}Sr_{2/3}FeO₃ exhibits a commensurate helimagnetic order with an ordering length of 13.4 Å [46, 47]. La-substitution, like oxygen vacancy formation, induces electron doping and a lattice expansion, so the microscopic origin may be similar. We note, however, that the chemical modification required is an order of magnitude larger with La-substitution (30%) than with oxygen vacancies to achieve a similar ordering length contraction. 3) We also note that CaFeO₃ exhibits incommensurate helimagnetic ordering with a length of 13.5–13.7 Å [16, 48]. CaFeO₃ is isovalent with SrFeO₃ but with a smaller lattice parameter. Crucially, CaFeO₃ is insulating while SrFeO₃ is metallic. In the case of Ca-substitution, the increased localization favors SE over DE and directly results in shorter ordering length. Oxygen stoichiometry may be comparatively less significant. 4) Lastly, a 5% substitution of cobalt for iron lengthens the helix up to 22 Å [11, 31]. Since SrCoO₃ is a ferromagnet, Co-substitution is expected to enhance the DE, which is consistent with our results.

Chemical modifications such as oxygen vacancies may also explain the spread of helimagnetic wavelength values reported in bulk SrFeO₃, shown as the gray markers in Fig. 3c, as well as differences between bulk and thin film samples, and between thin films prepared by different means. Thin films may be more susceptible to oxygen loss than bulk samples, owing to their higher surface area

to volume ratio, and samples synthesized and processed in different conditions may not be chemically identical. We note, however, that within the series of samples grown by MBE and annealed in oxygen plasma, and within the series of samples grown by PLD and annealed in ozone plasma, the trend of ordering length with strain is robust.

Despite the extreme strain effect on the spiral structure itself, the transition temperature from paramagnetic to helimagnetic remains at the bulk value of 120 K, independent of strain. This is also in contrast to conventional, DMI-based, helimagnets, where biaxial strain is reported to stabilize the helimagnetic phase towards higher temperatures, and again, highlights the fundamentally different physics at play in SrFeO_3 .

Our finding that the helimagnetic ordering length can be tuned by biaxial strain has direct implications for future SrFeO_3 -based devices. Since topologically protected skyrmion-like magnetic structures have a size governed by the underlying helimagnetic order, the ability to engineer their size and distribution is valuable for the development of high density magnetic memories with inherent topological protection. This finding is also crucial for engineering high-energy magnonic devices, since the magnon energy is inversely proportional to the helimagnetic spiral length.

Finally, our observations suggest a possible reconfigurable strategy to manipulate helimagnetic spin textures based on the high mobility of oxygen in SrFeO_x . Indeed, SrFeO_x compounds are widely studied for their superior oxygen-ion transport properties and potential application in neuromorphic hardware [49, 50]. In particular, electric field is found to drive a phase transition between the perovskite phase and the brownmillerite $\text{SrFeO}_{2.5}$ that can be reversed by oxygen annealing [49]. A similar electrostatic approach could be employed here to fine-tune the helimagnetic ordering *in situ*, offering an alternative to successful magnetoelectric-based tuning e.g. in BiFeO_3 [51].

In conclusion, we report that the magnetic ground state of SrFeO_3 thin films is analogous to prior reports from bulk samples but that biaxial tensile strain significantly shortens the helimagnetic ordering length. We attribute these changes to robust strain-induced modifications in stoichiometry leading to enhanced superexchange interactions. The effect is promising as an engineering strategy towards functional helimagnetic devices for spintronic, magnonic and quantum information applications. Finally, the strain tuning may be general to other chemically-tunable helimagnets and may provide a platform to understand the origins of this complex ordering in a broad class of quantum materials.

V. METHODS

Sample preparation – PLD

Thin film samples were grown by pulsed laser deposition by a KrF excimer laser of 248 nm wavelength operating at 3 Hz. The laser fluence was calculated to be 0.97 J cm^{-2} . The target was a pressed powder of $\text{SrFeO}_{2.5}$. Samples were grown in 50 mTorr of flowing oxygen at 620°C . 2 nm SrTiO_3 capping layers were grown *in-situ* at the same conditions as, and immediately following, $\text{SrFeO}_{2.5}$. A single crystal of SrTiO_3 served as the target. Warm up and cool down were ramps of 100°C per minute and were carried out in the same oxygen partial pressure as the growth. Ex-situ ozone anneal was performed at 200 - 260°C for 0.5 to 3 hours in a UV-assisted ozone plasma generator.

Sample preparation – MBE

Thin films were grown via molecular beam epitaxy in an ultra high vacuum chamber with base pressure equal to 3×10^{-7} mTorr. During the deposition, we maintained the substrate temperature at 650°C in a 4.5×10^{-3} mTorr oxygen background pressure. To completely oxidize the samples, we annealed them up to 600°C in a 0.01 mTorr oxygen plasma atmosphere and then cooled down slowly under the same conditions.

In-house x-ray diffraction

θ - 2θ measurements were acquired on a PANalytical X'Pert 2 Pro, a Bruker D8 Discover, or a Rigaku Smartlab diffractometer. Reciprocal space maps were acquired on a PANalytical Empyrean.

Neutron diffraction

The samples were measured in the [hh \bar{l}] scattering plane with the (hh \bar{l}) direction positioned at low scattering angle ($\theta \approx 20^\circ$) to access and optimize the magnetic satellites with respect to the neutron flux.

Resonant soft x-ray scattering

The temperature-dependent θ - 2θ scans were performed using an in-vacuum four circle goniometer at the Resonant Elastic and Inelastic X-ray Scattering (REIXS) beamline of the Canadian Light Source (CLS) [52]. The samples were mounted on a wedge of 54.7° and rotated around the surface normal by 45° to orient the [111] direction in the horizontal diffraction plane. The scattered x-rays were detected using a silicon drift detector. The ordering

length is obtained by fitting the peaks with Gaussian lineshapes and extracting the center.

Density functional theory

We perform first-principles density functional calculations within the Perdew–Burke–Ernzerhof exchange–correlation functional revised for solid (PBEsol) [53] as implemented in the Vienna *Ab initio* Simulation Package (VASP) with the projector augmented wave (PAW) method [54–59]. The core and valence electrons are treated using the following electronic configurations: $4s^24p^65s^2$ (Sr), $3d^74s^1$ (Fe), $2s^22p^4$ (O), and a 600 eV plane wave cutoff. Calculations were carried out using the experimental lattice parameters, while internal distortions were neglected since none are observed experimentally. The Brillouin zone was sampled with a $12 \times 12 \times 12$ Gamma-centered k-point mesh. For the noncollinear spin-order calculations, the wave function is expressed as a spinor, and a generalized Bloch boundary condition is applied [60]. To stabilize the helical spin configuration, the on-site Coulomb interaction U and Hund’s exchange interaction J_H are included [19]. In this study, we use $U = 3.0$ eV and $J_H = 1.0$ eV. The electronic effect of oxygen deficiency is simulated using the background-charge approach, in which the total number of electrons is tuned, and charge neutrality is enforced by a uniform compensating background.

Multiplet calculations

Hybridized ligand field multiplet calculations were carried out following our previous work, utilizing a reduced metal cluster with two ligands along the X and Y directions [61]. Parameters were set based on calculations of other octahedral iron oxide compounds [62] and are reported in the SI Section 8.

ACKNOWLEDGMENTS

The work at SLAC/Stanford was supported by the US Department of Energy, Office of Basic Energy Sciences, Division of Materials Sciences and Engineering, under contract no. DE-AC02-76SF00515. SJM was supported by the Army Research Office, Grant No. W911NF-15-1-0133. LB thanks São Paulo Research Foundation - FAPESP for the financial support (Grant 2018/25718-5). Part of the research described in this paper was performed at the Canadian Light Source, a national research facility of the University of Saskatchewan, which is supported by the Canada Foundation for Innovation (CFI), the Natural Sciences and Engineering Research Council (NSERC), the Canadian Institutes of Health Research (CIHR), the Government of Saskatchewan, and the University of Saskatchewan. Part of this work was performed at the Stanford Nano Shared Facilities (SNSF) RRID:SCR_023230, supported by the National Science Foundation under award ECCS-2026822. Computational work at Northwestern was supported by the Department of Energy, Office of Science FWP-101256 as part of the Enabling Science for Transformative Energy-Efficient Microelectronics (ESTEEM) Center. Multiplet calculations were performed on the Sherlock cluster at Stanford University and on resources of the National Energy Research Scientific Computing Center (NERSC), a Department of Energy Office of Science User Facility, using NERSC award BES-ERCAP0027203.

[1] R. Islam, P. Li, M. Beg, M. Sachdev, and G. X. Miao, Helimagnet-based nonvolatile multi-bit memory units, *Applied Physics Letters* **122**, 152407 (2023).

[2] C. Psaroudaki, E. Peraticos, and C. Panagopoulos, Skyrmion qubits: Challenges for future quantum computing applications, *Applied Physics Letters* **123**, 260501 (2023).

[3] S. Hayami, Mechanism of antisymmetric spin polarization in centrosymmetric multiple-Q magnets based on effective chiral bilinear and biquadratic spin cross products, *Physical Review B* **105**, 024413 (2022).

[4] E. W. Hodt, H. Bentmann, and J. Linder, Fate of p -wave spin polarization in helimagnets with Rashba spin-orbit coupling, *Physical Review B* **111**, 205416 (2025).

[5] S. Mühlbauer, B. Binz, F. Jonietz, C. Pfleiderer, A. Rosch, A. Neubauer, R. Georgii, and P. Böni, Skyrmion lattice in a chiral magnet, *Science* **323**, 915 (2009).

[6] X. Z. Yu, Y. Onose, N. Kanazawa, J. H. Park, J. H. Han, Y. Matsui, N. Nagaosa, and Y. Tokura, Real-space observation of a two-dimensional skyrmion crystal, *Nature* **465**, 901 (2010).

[7] T. Kurumaji, T. Nakajima, M. Hirschberger, A. Kikkawa, Y. Yamasaki, H. Sagayama, H. Nakao, Y. Taguchi, T. hisa Arima, and Y. Tokura, Skyrmion lattice with a giant topological Hall effect in a frustrated triangular-lattice magnet, *Science* **365**, 914 (2019).

[8] T. Takeda, Y. Yamaguchi, and H. Watanabe, Magnetic Structure of SrFeO_3 , *Journal of the Physical Society of Japan* **33**, 967 (1972).

[9] M. Mostovoy, Helicoidal ordering in iron perovskites, *Physical Review Letters* **94**, 137205 (2005).

[10] S. Ishiwata, M. Tokunaga, Y. Kaneko, D. Okuyama, Y. Tokunaga, S. Wakimoto, K. Kakurai, T. Arima, Y. Taguchi, and Y. Tokura, Versatile helimagnetic phases under magnetic fields in cubic perovskite SrFeO_3 , *Physical Review B* **84**, 054427 (2011).

[11] S. Chakraverty, T. Matsuda, H. Wadati, J. Okamoto, Y. Yamasaki, H. Nakao, Y. Murakami, S. Ishiwata, M. Kawasaki, Y. Taguchi, Y. Tokura, and H. Y. Hwang, Multiple helimagnetic phases and topological Hall effect in epitaxial thin films of pristine and Co-doped SrFeO_3 , *Physical Review B* **88**, 220405(R) (2013).

[12] M. Onose, H. Takahashi, H. Sagayama, Y. Yamasaki, and S. Ishiwata, Complete phase diagram of $\text{Sr}_{1-x}\text{La}_x\text{FeO}_3$ with versatile magnetic and charge ordering, *Physical Review Materials* **4**, 114420 (2020).

[13] S. Ishiwata, T. Nakajima, J. H. Kim, D. S. Inosov, N. Kanazawa, J. S. White, J. L. Gavilano, R. Georgii, K. M. Seemann, G. Brandl, P. Manuel, D. D. Khalyavin, S. Seki, Y. Tokunaga, M. Kinoshita, Y. W. Long, Y. Kaneko, Y. Taguchi, T. Arima, B. Keimer, and Y. Tokura, Emergent topological spin structures in the centrosymmetric cubic perovskite SrFeO_3 , *Physical Review B* **101**, 134406 (2020).

[14] J. M. Rondinelli and N. A. Spaldin, Electron-lattice instabilities suppress cuprate-like electronic structures in $\text{SrFeO}_3/\text{SrTiO}_3$ superlattices, *Physical Review B* **81**, 085109 (2010).

[15] R. J. Green and G. A. Sawatzky, Negative Charge Transfer Energy in Correlated Compounds, *Journal of the Physical Society of Japan* **93**, 121007 (2024).

[16] P. C. Rogge, R. J. Green, R. Sutarto, and S. J. May, Itinerancy-dependent noncollinear spin textures in SrFeO_3 , CaFeO_3 , and $\text{CaFeO}_3/\text{SrFeO}_3$ heterostructures probed via resonant X-ray scattering itinerancy-dependent noncollinear spin, *Physical Review Materials* **3**, 084404 (2019).

[17] P. C. Rogge, P. Shafer, G. Fabbri, W. Hu, E. Arenholz, E. Karapetrova, M. P. M. Dean, R. J. Green, and S. J. May, Depth-Resolved Modulation of Metal – Oxygen Hybridization and Orbital Polarization across Correlated Oxide Interfaces, *Advanced Materials* **31**, 1902364 (2019).

[18] D. Takegami, M. Nakamura, A. Melendez-Sans, K. Fujinuma, R. Nakamura, M. Yoshimura, K. D. Tsuei, A. Tanaka, M. Gen, Y. Tokunaga, S. Ishiwata, and T. Mizokawa, Negative charge-transfer energy in SrFeO_3 revisited with hard x-ray photoemission spectroscopy, *Physical Review B* **109**, 235138 (2024).

[19] Z. Li, R. Laskowski, T. Iitaka, and T. Tohyama, First-principles calculation of helical spin order in iron perovskite SrFeO_3 and BaFeO_3 , *Physical Review B* **85**, 134419 (2012).

[20] S. X. Huang and C. L. Chien, Extended Skyrmiion Phase in Epitaxial $\text{FeGe}(111)$ Thin Films, *Physical Review Letters* **108**, 267201 (2012).

[21] S. Seki, Y. Okamura, K. Shibata, R. Takagi, N. D. Khanh, F. Kagawa, T. Arima, and Y. Tokura, Stabilization of magnetic skyrmions by uniaxial tensile strain, *Physical Review B* **96**, 220404(R) (2017).

[22] S. Budhathoki, A. Sapkota, K. M. Law, S. Ranjit, B. D. Hoskins, A. S. Thind, A. Y. Borisevich, M. E. Jamer, T. J. Anderson, A. D. Koehler, K. D. Hobart, G. M. Stephen, D. Heiman, T. Mewes, R. Mishra, J. C. Gallagher, and A. J. Hauser, Room-temperature skyrmions in strain-engineered FeGe thin films, *Physical Review B* **101**, 220405(R) (2020).

[23] A. Chacon, A. Bauer, T. Adams, F. Rucker, G. Brandl, R. Georgii, M. Garst, and C. Pfleiderer, Uniaxial Pressure Dependence of Magnetic Order in MnSi , *Physical Review Letters* **115**, 267202 (2015).

[24] B. Fåk, R. A. Sadykov, J. Flouquet, and G. Lapertot, Pressure dependence of the magnetic structure of the itinerant electron magnet MnSi , *J. Phys. Condens. Matt.* **17**, 1635 (2005).

[25] L. J. Bannenberg, R. Sadykov, R. M. Dalgliesh, C. Goodway, D. L. Schlagel, T. A. Lograsso, P. Falus, A. O. Leonov, and C. Pappas, Skyrmions and spirals in MnSi under hydrostatic pressure, *Physical Review B* **100**, 054447 (2019).

[26] D. Sando, A. Agbelele, D. Rahmedov, J. Liu, P. Rovilain, C. Toulouse, I. C. Infante, A. P. Pyatakov, S. Fusil, E. Jacquet, C. Carrétéro, C. Deranlot, S. Lisenkov, D. Wang, J.-M. Le Breton, M. Cazayous, A. Sacuto, J. Juraszek, A. K. Zvezdin, L. Bellaiche, B. Dkhil, A. Barthélémy, and M. Bibes, Crafting the magnonic and spintronic response of BiFeO_3 films by epitaxial strain, *Nat Mater* **12**, 641 (2013).

[27] S. R. Burns, D. Sando, B. Xu, B. Dupé, L. Russell, G. Deng, R. Clements, O. H. C. Paull, J. Seidel, L. Bellaiche, N. Valanoor, and C. Ulrich, Expansion of the spin cycloid in multiferroic BiFeO_3 thin films, *npj Quantum Materials* **4**, 18 (2019).

[28] K. Shimamoto, S. Mukherjee, S. Manz, J. S. White, M. Trassin, M. Kenzelmann, L. Chapon, T. Lippert, M. Fiebig, C. W. Schneider, and C. Niedermayer, Tuning the multiferroic mechanisms of TbMnO_3 by epitaxial strain, *Scientific Reports* **7**, 44753 (2017).

[29] L. C. Chapon, P. Manuel, P. G. Radaelli, C. Benson, L. Perrott, S. Ansell, N. J. Rhodes, D. Raspino, D. Duxbury, E. Spill, and J. Norris, Wish: The New Powder and Single Crystal Magnetic Diffractometer on the Second Target Station, *Neutron News* **22**, 22 (2011).

[30] M. Reehuis, C. Ulrich, A. Maljuk, C. Niedermayer, B. Ouladdiaf, A. Hoser, T. Hofmann, and B. Keimer, Neutron diffraction study of spin and charge ordering in $\text{SrFeO}_{3-\delta}$, *Physical Review B* **85**, 184109 (2012).

[31] Y. W. Long, Y. Kaneko, S. Ishiwata, Y. Tokunaga, T. Matsuda, H. Wadati, Y. Tanaka, S. Shin, Y. Tokura, and Y. Taguchi, Evolution of magnetic phases in single crystals of $\text{SrFe}_{1-x}\text{Co}_x\text{O}_3$ solid solution, *Physical Review B* **86**, 064436 (2012).

[32] S. Nasu, K. Wada, T. Abe, K. Yamamoto, S. Endo, M. Takano, and Y. Takeda, High-pressure Mössbauer study of perovskite iron oxides, *Nuclear Inst. and Methods in Physics Research, B* **76**, 185 (1993).

[33] Z. Li, T. Iitaka, and T. Tohyama, Pressure-induced ferromagnetism in cubic perovskite SrFeO_3 and BaFeO_3 , *Physical Review B* **86**, 094422 (2012).

[34] J. C. Slater and G. F. Koster, Simplified LCAO method for the periodic potential problem, *Physical Review* **94**, 1498 (1954).

[35] J. B. Goodenough, Theory of the Role of Covalence in the Perovskite-Type Manganites $[\text{La},\text{M}(\text{II})]\text{MnO}_3$, *Physical Review* **100**, 564 (1955).

[36] J. Kanamori, Superexchange interaction and symmetry properties of electron orbitals, *Journal of Physics and Chemistry of Solids* **10**, 87 (1959).

[37] P. W. Anderson, Antiferromagnetism. Theory of Superexchange Interaction, *Physical Review* **79**, 350 (1950).

[38] M. V. Mostovoy and D. I. Khomskii, Orbital Ordering in Charge Transfer Insulators, *Physical Review Letters* **92**, 167201 (2004).

[39] L. J. Ford, P. R. Slater, J. K. Christie, and P. Goddard, Carbon dioxide and water incorporation mechanisms in SrFeO_3 phases : a computational study, *Physical Chemistry Chemical Physics* **22**, 25146 (2020).

[40] O. I. Lebedev, J. Verbeeck, G. V. Tendeloo, N. Hayashi, and T. Terashima, Structure and microstructure of epitaxial $\text{Sr}_n\text{Fe}_n\text{O}_{3n-1}$ films, *Philosophical Magazine* **84**, 3825 (2004).

[41] T. Mayeshiba and D. Morgan, Strain effects on oxygen vacancy formation energy in perovskites, *Solid State Ionics* **311**, 105 (2017).

[42] U. Aschauer, R. Pfenninger, S. M. Selbach, T. Grande, and N. A. Spaldin, Strain-controlled oxygen vacancy formation and ordering in CaMnO_3 , *Physical Review B* **88**, 054111 (2013).

[43] K. S. Takahashi, Y. Matsubara, M. S. Bahramy, N. Ogawa, D. Hashizume, and Y. Tokura, Polar metal phase stabilized in strained La-doped BaTiO_3 films, *Scientific Reports* **7**, 4631 (2017).

[44] X. Chen and T. Grande, Anisotropic and Nonlinear Thermal and Chemical Expansion of $\text{La}_{1-x}\text{Sr}_x\text{FeO}_{3-\delta}$, *Chemistry of Materials* **25**, 3296 (2013).

[45] J. P. Palakkal, L. Zeinar, M. Major, P. Komissinskiy, T. Schneider, and L. Alff, Thickness-Dependent Magnetism in Epitaxial $\text{SrFeO}_{3-\delta}$ Thin Films, *IEEE Transactions on Magnetics* **57**, 2200105 (2021).

[46] J. Okamoto, D. J. Huang, K. S. Chao, S. W. Huang, C. Hsu, A. Fujimori, A. Masuno, T. Terashima, M. Takano, and C. T. Chen, Quasi-two-dimensional d -spin and p -hole ordering in the three-dimensional perovskite $\text{La}_{1/3}\text{Sr}_{2/3}\text{FeO}_3$, *Physical Review B* **82**, 132402 (2010).

[47] J. Ma, J. Yan, S. O. Diallo, R. Stevens, A. Llobet, F. Trouw, D. L. Abernathy, M. B. Stone, and R. J. Mcqueeny, Role of magnetic exchange energy on charge ordering in $\text{R}_{1/3}\text{Sr}_{2/3}\text{FeO}_3$ ($\text{R} = \text{La}$, Pr , and Nd), *Physical Review B* **84**, 224115 (2011).

[48] P. Woodward, D. Cox, E. Moshopoulou, A. W. Sleight, and S. Morimoto, Structural studies of charge disproportionation and magnetic order in CaFeO_3 , *Physical Review B* **62**, 844 (2000).

[49] V. R. Nallagatla, T. Heisig, C. Baeumer, V. Feyer, M. Juggovac, G. Zamborlini, C. M. Schneider, R. Waser, M. Kim, C. U. Jung, and R. Dittmann, Topotactic Phase Transition Driving Memristive Behavior, *Advanced Materials* **31**, 1903391 (2019).

[50] C. Ge, C.-x. Liu, Q.-l. Zhou, Q.-h. Zhang, J.-y. Du, J.-k. Li, C. Wang, L. Gu, G.-z. Yang, and K.-j. Jin, A Ferrite Synaptic Transistor with Topotactic Transformation, *Advanced Materials* **31**, 1900379 (2019).

[51] P. Rovillain, R. D. Sousa, Y. Gallais, A. Sacuto, M. A. Méasson, D. Colson, A. Forget, M. Bibes, A. Barthélémy, and M. Cazayous, Electric-field control of spin waves at room temperature in multiferroic BiFeO_3 , *Nature Materials* **9**, 975 (2010).

[52] D. G. Hawthorn, F. He, L. Venema, H. Davis, A. J. Achkar, J. Zhang, R. Sutarto, H. Wadati, A. Radi, T. Wilson, G. Wright, K. M. Shen, J. Geck, H. Zhang, V. Novák, and G. A. Sawatzky, An in-vacuum diffractometer for resonant elastic soft x-ray scattering, *Review of Scientific Instruments* **82**, 073104 (2011).

[53] J. P. Perdew, A. Ruzsinszky, G. I. Csonka, O. A. Vydrov, G. E. Scuseria, L. A. Constantin, X. Zhou, and K. Burke, Restoring the density-gradient expansion for exchange in solids and surfaces, *Physical Review Letters* **100**, 136406 (2008).

[54] G. Kresse and J. Hafner, Ab initio molecular dynamics for liquid metals, *Physical Review B* **47**, 558 (1993).

[55] G. Kresse and J. Furthmüller, Efficiency of ab-initio total energy calculations for metals and semiconductors using a plane-wave basis set, *Computational Materials Science* **6**, 15 (1996).

[56] G. Kresse and J. Furthmüller, Efficient iterative schemes for ab initio total-energy calculations using a plane-wave basis set, *Physical Review B* **54**, 11169 (1996).

[57] J. P. Perdew, K. Burke, and M. Ernzerhof, Generalized gradient approximation made simple, *Physical Review Letters* **77**, 3865 (1996).

[58] P. E. Blöchl, Projector augmented-wave method, *Physical Review B* **50**, 17953 (1994).

[59] G. Kresse and D. Joubert, From ultrasoft pseudopotentials to the projector augmented-wave method, *Physical Review B* **59**, 1758 (1999).

[60] L. M. Sandratskii, Energy band structure calculations for crystals with spiral magnetic structure, *physica status solidi (b)* **136**, 167 (1986).

[61] E. G. Lomeli, Q. Li, K. H. Hsu, G.-h. Lee, Z. Zhuo, B.-j. Polzin, J. Gim, B. Shi, E. Lee, Y. Wang, H. Li, P. Yu, J. Wu, Z.-x. Shen, S. Yan, L. Illa, J. J. Kas, J. J. Rehr, J. Vinson, B. Moritz, Y.-s. Liu, J. Guo, Y.-d. Chuang, W. Yang, and T. P. Devereaux, Negative Charge Transfer: Ground State Precursor towards High Energy Batteries, *arXiv cond-mat* , 2509.20622v1 (2025).

[62] H. Ramachandran, E. W. Mu, E. G. Lomeli, A. Braun, M. Goto, K. H. Hsu, J. Liu, Z. Jiang, K. Lim, G. M. Busse, B. Moritz, J. J. Kas, J. Vinson, J. J. Rehr, J. Park, I. I. Abate, Y. Shimakawa, E. I. Solomon, W. Yang, W. E. Gent, T. p. Devereaux, and W. C. Chueh, A formal $\text{Fe}^{III/V}$ redox couple in an intercalation electrode, *Nature Materials* **25**, 91 (2025).